

FIRST COSMIC SHEAR RESULTS FROM THE CANADA-FRANCE-HAWAII TELESCOPE WIDE SYNOPTIC LEGACY SURVEY[†]

H. HOEKSTRA¹, Y. MELLIER^{2,3}, L. VAN WAERBEKE⁴, E. SEMBOLONI², L. FU², M.J. HUDSON⁵, L.C. PARKER⁵, I. TERENO^{2,6},
& K. BENABED^{2,3}

Draft version April 14, 2018

ABSTRACT

We present the first measurements of the weak gravitational lensing signal induced by the large scale mass distribution from data obtained as part of the ongoing Canada-France-Hawaii Telescope Legacy Survey (CFHTLS). The data used in this analysis are from the Wide Synoptic Survey, which aims to image ~ 170 square degree in five filters. We have analysed $\sim 22 \text{ deg}^2$ (31 pointings) of i' data spread over two of the three survey fields. These data are of excellent quality and the results bode well for the remainder of the survey: we do not detect a significant ‘B’-mode, suggesting that residual systematics are negligible at the current level of accuracy. Assuming a Cold Dark Matter model and marginalising over the Hubble parameter $h \in [0.6, 0.8]$, the source redshift distribution and systematics, we constrain σ_8 , the amplitude of the matter power spectrum. At a fiducial matter density $\Omega_m = 0.3$ we find $\sigma_8 = 0.85 \pm 0.06$. This estimate is in excellent agreement with previous studies. Combination of our results with those from the Deep component of the CFHTLS enables us to place a constraint on a constant equation of state for the dark energy, based on cosmic shear data alone. We find that $w_0 < -0.8$ at 68% confidence.

Subject headings: cosmology: observations – dark matter – gravitational lensing

1. INTRODUCTION

Weak gravitational lensing of distant galaxies by intervening massive structures in the universe provides us with a unique, and unbiased way to study the distribution of matter in the universe. Although weak lensing has many applications in astronomy, from the study of galaxy dark matter halos (e.g., Brainerd et al. 1996; Hudson et al. 1998; McKay et al. 2001; Hoekstra et al. 2004) to galaxy clusters (e.g., Clowe et al. 1998; Dahle et al. 2002; Hoekstra et al. 2002a; Cypriano et al. 2004), much recent work has been devoted to the measurement of the statistical signal induced by large scale structure (a.k.a. cosmic shear).

The reason for the recent popularity of cosmic shear is the fact that the signal is a direct measure of the projected matter power spectrum over a redshift range determined by the lensed sources and over scales ranging from the linear to non-linear regime. This straightforward in-

terpretation of the signal is rather unique in the growing set of tools available for cosmology, and is an important feature if we are to determine the values of cosmological parameters with high precision. It enables us to measure important parameters such as the matter density Ω_m and the amplitude of the power spectrum σ_8 , but also has the potential to constrain quintessence models (Benabed & van Waerbeke 2004; Tereno et al., in preparation). The combination of cosmic shear with other well understood probes, such as the cosmic microwave background (CMB) is particularly powerful (e.g., Contaldi et al. 2003; Tereno et al. 2005).

The measurement of the signal, however, is not without challenges, which explains why cosmic shear has only recently appeared as a useful tool in cosmology. First of all, the induced change in the shapes of distant galaxies is small (less than 1%), much smaller than the intrinsic shapes of the sources themselves. As a result, large areas of the sky need to be surveyed in order to reduce the statistical errors. The first detections, reported only a few years ago (Bacon, Refregier & Ellis 2000; Kaiser, Wilson & Luppino 2000; van Waerbeke et al. 2000; Wittman et al. 2000), were based on relatively small areas (few deg^2 at most). Recent developments in the construction of wide field imaging cameras on 4m+ class telescopes have made it possible to image much larger portions on the sky to warrant accurate measurements of the lensing signal. For instance, van Waerbeke, Mellier & Hoekstra (2005) presented results based on $\sim 12 \text{ deg}^2$ of deep imaging data from the VIRMOS-Descart Survey. Other competitive results are based on shallower data, which cover a larger area, such as the Red-sequence Cluster Survey (RCS; Hoekstra et al., 2002c) based on 53 deg^2 and the 75 deg^2 CTIO Lensing Survey (e.g., Jarvis et al. 2003; Jarvis et al. 2005).

The second challenge is the careful removal of observational distortions, introduced by the telescope optics and

[†] Based on observations obtained with MegaPrime equipped with MegaCam, a joint project of CFHT and CEA/DAPNIA, at the Canada-France-Hawaii Telescope (CFHT) which is operated by the National Research Council (NRC) of Canada, the Institut National des Sciences de l’Univers of the Centre National de la Recherche Scientifique (CNRS) of France, and the University of Hawaii. This work is based in part on data products produced at TERAPIX and the Canadian Astronomy Data Centre as part of the Canada-France-Hawaii Telescope Legacy Survey, a collaborative project of NRC and CNRS.

¹ Department of Physics and Astronomy, University of Victoria, Victoria, BC, V8P 5C2, Canada

² Institut d’Astrophysique de Paris, 98bis Boulevard Arago, 75014 Paris, France

³ Observatoire de Paris, LERMA, 61 avenue de l’Observatoire, 75014 Paris, France

⁴ Department of Physics and Astronomy, University of British Columbia, Vancouver, BC, V6T 1Z1, Canada

⁵ Department of Physics, University of Waterloo, Waterloo, ON, N2L 3G1, Canada

⁶ Departamento de Física, Universidade de Lisboa, 1749-016 Lisboa, Portugal

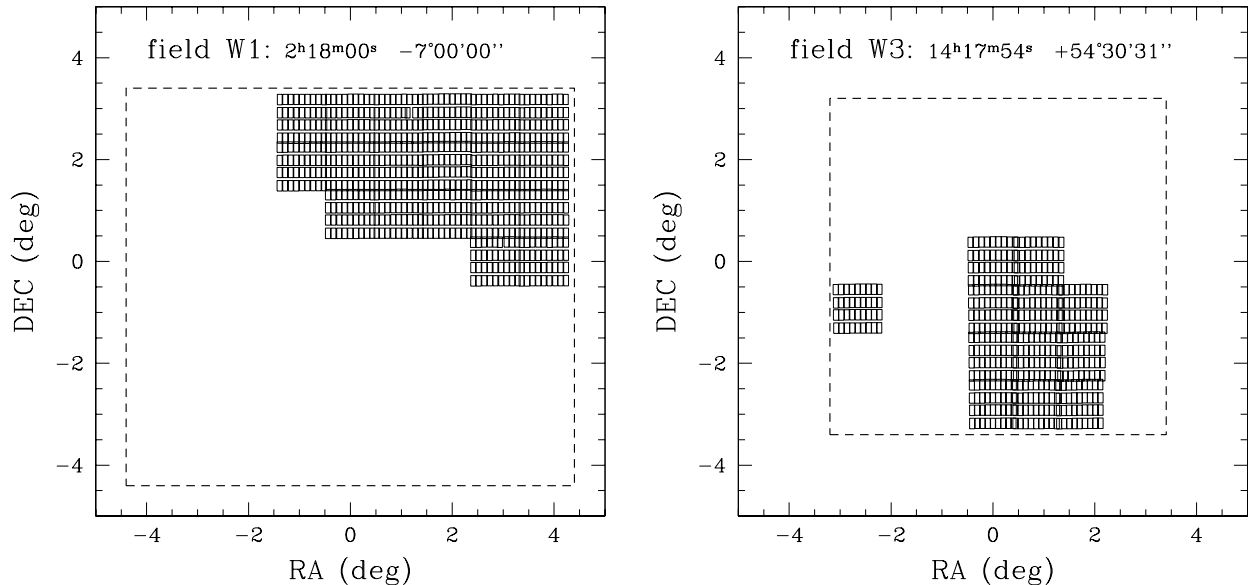


FIG. 1.— Layout of the observations of the W1 and W3 field. Each rectangle corresponds to one of the MegaCam chips. The dashed box indicates the planned size of each of the two fields, 72 deg^2 for W1 and 49 deg^2 for W3. Currently 19 deg^2 of W1 and 12 deg^2 of W3 have been observed.

atmosphere. Much work has been devoted to deal with the point spread function (PSF) and several correction schemes have been developed (e.g., Kaiser et al. 1995; Bernstein & Jarvis 2002; Refregier 2003) and tested (e.g., see Heymans et al. 2005 for the most up to date discussion). Fortunately the separation of the signal into gradient (‘E’-mode) and curl (‘B’-mode) components provides a non-trivial test of the level of residual systematics, including the presence of intrinsic alignments of galaxies or observational distortions in the images. In addition, several other tests can be performed to test the accuracy of the corrections (e.g., Hoekstra et al. 2002b; Bacon et al. 2003; Heymans 2003; van Waerbeke et al. 2005; Heymans et al. 2005). The recent results presented in van Waerbeke et al. (2005) and Jarvis & Jain (2005) have demonstrated that these systematics can be accurately corrected for, resulting in measurements free of ‘B’-modes.

The next step is to survey much larger areas on the sky to sufficient depth in multiple filters, which enables us to probe the evolution of the matter power spectrum. The Canada-France-Hawaii-Telescope Legacy Survey (CFHTLS) aims to image ~ 170 square degree in the i' -filter down to $i'_{AB} = 24.5$. This is comparable to the depth reached in the VIRMOS-Descart survey, but an order of magnitude larger in survey area, thus resulting in a significant reduction in statistical errors. In addition, the fields are observed in 4 additional filters as to ensure photometric redshift information for the sources. This is an important part of the survey, as it enables tests for intrinsic alignments and the study of the evolution of the matter power spectrum. The latter significantly improves the constraints on cosmological parameters, in particular on the equation of state of the dark energy (Benabed & van Waerbeke 2004)

In this paper we present the first results from the CFHTLS cosmic shear program, based on 31 pointings,

resulting in an effective area of $\sim 22 \text{ deg}^2$ of i' data, already a significant increase compared to previous work. The structure of the paper is as follows. In §2 we discuss the CFHTLS and the data used in this paper as well as the data reduction process. The weak lensing analysis is described in §3. The resulting cosmic shear signal is presented in §4 and the implications for cosmological parameters are discussed in §5.

2. DATA

The Canada-France-Hawaii Telescope Legacy Survey (CFHTLS)¹ is a joint Canadian-French program to make efficient use of Megaprime, the CFHT wide field imager, and to address a number of fundamental problems in astronomy. Megaprime, equipped with MegaCam, a 36 CCD mosaic camera with a field of view of $\sim 1 \text{ deg}^2$, enables us to obtain deep images of large areas of the sky. The survey itself consists of three independent parts, each with their own primary science driver. The survey has been allocated more than 450 nights over a ~ 5 year period.

The results presented in this paper deal with data collected as part of the wide synoptic survey, or ‘Wide Survey’ for short. Once completed, it will cover $\sim 170 \text{ deg}^2$ in three patches of 49 to 72 square degrees through the whole filter set (u^* , g^* , r^* , i' , z') down to $i'=24.5$. The survey allows the study of the large scale structures and matter distribution in the universe through weak lensing and the galaxy distribution. The former application is the focus of this paper. We also use cosmic shear results based on multi-color data from the Deep component of the survey, which are described in detail in Semboloni et al. (2005).

For the analysis presented here we use 19 pointings in the i' -band from the W1-field and 12 pointings from the W3-field, resulting in an effective survey area 22 deg^2

¹ <http://www.cfht.hawaii.edu/Science/CFHLS>

after masking. The layout of the current data with respect to the final survey is presented in Figure 1. These data were obtained during the 2003B, 2004A and 2004B observing semesters. In addition, 4 deg² of the W2 field have been observed, but the area is not contiguous and we omit these data from the current analysis.

2.1. Data Reduction

Detrended data (de-biased and flatfielded) are provided by CFHT to the community through the Canadian Astronomical Data Centre (CADC). The detrending is done using the Elixir pipeline developed at CFHT. The pipeline also provides photometric zeropoints and in most cases a reasonable first order astrometric solution.

The photometric calibrations are based on observations of standard stars during the observing run. These zeropoints are only valid under photometric conditions. We therefore examine the magnitudes of a large number of objects in the images, to check the stability of the photometric zero-point and scale the images to the brightest image. Most data were taken under photometric conditions, and the corrections are found to be small.

The astrometric solutions provided by the Elixir pipeline are more reliable for the more recent data, whereas a small fraction of chips of the earliest observations require a significant revision of the initial astrometry. The provided astrometric solution, however, is not accurate enough for the purpose of our study and needs to be improved upon. This process is too time consuming to be done manually, and is done using an additional pipeline. The USNO-A2 catalog could be used to refine the astrometry, but the number density of sources is often too low to warrant stable results. Instead, retrieved a red image from the second generation Digital Sky Survey (POSS II) for each pointing. These observations have small geometric distortions. The astrometry of the POSS II image is calibrated using the USNO-A2 catalog. SExtractor (Bertin & Arnouts 1996) is used to generate a catalog of sources with accurate astrometry, with a number density significantly higher than the USNO-A2 catalog. In addition, the POSS II images have been taken more recently, thus reducing the effects of proper motions of the stars.

This new astrometric catalog is matched to each of the MegaCam images. The exposures have been taken with different offsets, in order to fill the gaps between the chips. We combine the matched catalogs for each exposure into a master catalog, which contains the average positions of the matched objects. This master catalog is used to derive the final second order astrometric solution for each chip. This procedure ensures that in the overlapping area, the objects in each exposure are accurately matched to the same position, which is crucial when stacking the images for a weak lensing analysis: errors in the astrometry lead to additional anisotropies in the images.

Tests show that the resulting astrometric solution for each pointing is sufficiently accurate to stack all data into a large image. However, in this case different chips can contribute to the image at a given position. If the PSF properties “jump” between chips, this gives rise to a complicated PSF anisotropy pattern. Instead, we use only those regions of the sky which in the final stacks were all observed by the same chip. This avoids complicated

behaviour of the PSF, at the expense of approximately 20% of the survey area. In the future we plan to investigate in more detail to what extent we can deal with the PSF on full mosaic images.

Before stacking the images, we identify stars on chip 22 (which has the best image quality; see Figure 2) and measure the FWHM of the PSF and PSF anisotropy. If the seeing of some of the exposures is significantly worse than the others, or if the images show extreme PSF anisotropy, those images are discarded before stacking the images. We stack each chip separately, using the SWarp routine. The resulting images are cropped such that the overlapping regions remain. These images are used in the weak lensing analysis presented here. Typically the stacked images consist of 7 images, each with an integration time of 620s, but because of reasons described above, in a few cases we end up with stacks of 6 images. The improvement in the PSF behaviour warrants the minor decrease in depth.

Figure 2 shows the seeing distribution (or PSF size) as measured from the stacked images. Panel a shows the distribution for stars selected on chip 22, which typically has the best image quality. For this particular chip we find a median seeing of 0''.71. Towards the edge of the field of view the image quality degrades and a more accurate representation of the PSF size distribution is presented in Figure 2b, which shows a histogram of the distribution based on all chips. In this case the median FWHM is 0''.76. We note that recent changes to Megaprime have led to a significant improvement in image quality and a large reduction in PSF anisotropy, thus reducing the level of systematics in future cosmic shear measurements.

Nevertheless, the image quality in these early data is better than 1 arcsecond for all data used here. Figure 2c shows the PSF size as a function of chip number for the best seeing image (filled circles) and worst seeing image (open squares). The camera consists of four rows of nine chips, which results in the “periodic” changes in the seeing. In both cases the PSF size is best in the middle of the camera and increases towards the edges.

3. WEAK LENSING ANALYSIS

The weak lensing analysis presented here is based on the method proposed by Kaiser et al. (1995) and Lupino & Kaiser (1997) with a number of modifications that are described in Hoekstra et al. (1998) and Hoekstra et al. (2000). This particular method has been tested in great detail (e.g., Hoekstra et al. 1998, 2002b; Bacon et al. 2001; Erben et al. 2001; Heymans et al. 2005) and is widely used for cosmic shear studies. Several promising alternative methods have been developed recently (e.g, Bernstein & Jarvis 2002; Refregier 2003) and tests are underway to ensure accurate measurements of the lensing signal.

Although the Kaiser et al. (1995) method is not the ‘ultimate’ technique to extract the lensing signal from the images, it has proven to be one of the most accurate techniques currently available when tested on simulated data as part of the Shear TEsting Programme (STEP; Heymans et al. 2005). In this experiment, various weak lensing pipelines were used to measure the shear in simulated images. The simulated data consisted of a series with 5 different shears (constant across the images)

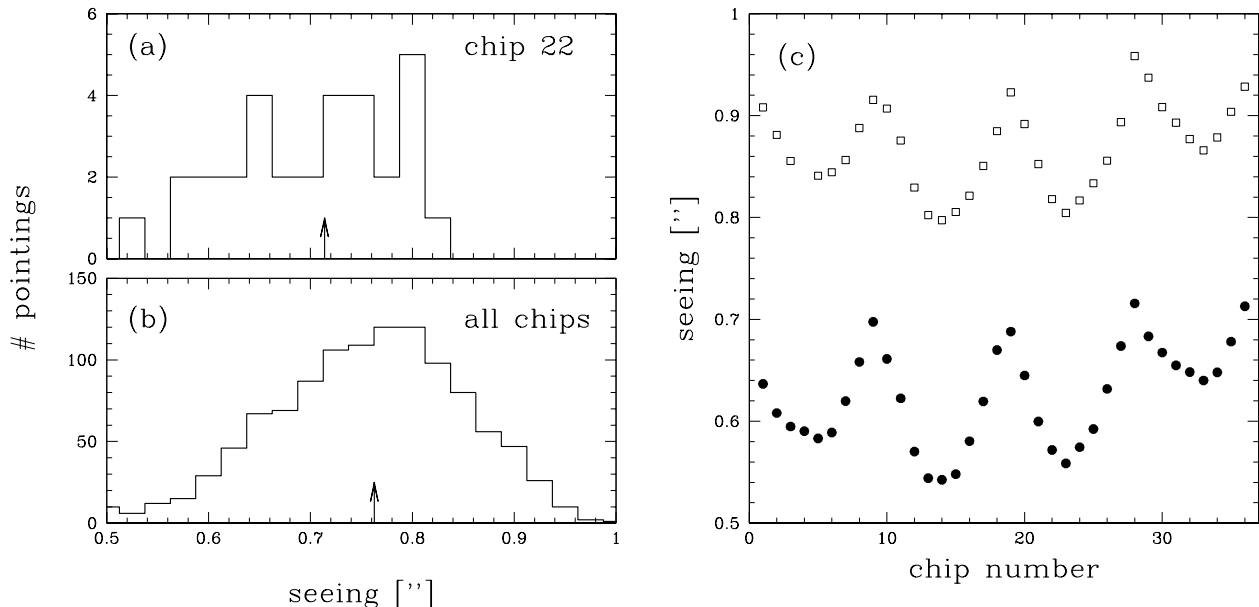


FIG. 2.— (a) FWHM of stars measured from the stacked images of chip 22 for all pointings. This chip typically has the best image quality (see panel c). (b) FWHM measured for all chips, providing a more accurate representation of the PSF size distribution. The arrows indicate the median seeing for both distributions. (c) The PSF size as a function of chip number for the best seeing image (filled circles) and the worst seeing image (open squares). The camera consists of 4 rows of 9 chips each. The image quality is best in the center of the camera, and degrades towards the edge as is indicated by these measurements.

and 5 different (fairly realistic) PSFs, each introducing different systematics. Hence STEP provides a test of how one can correct for both PSF anisotropy and the size of the PSF. However, the simulations do not capture all details of real PSFs or imperfections introduced by the stacking process. In this experiment, the Hoekstra et al. (1998; 2000) implementation of the Kaiser et al. (1995) approach was able to recover the lensing signal with an accuracy better than 2%. This accuracy is sufficient for published cosmic shear results, and acceptable for the results presented here, but we note that improvements are likely to be needed when analysing the complete CFHTLS data set.

As mentioned earlier, we analyse the stacked images for each chip individually. The first step in the analysis is the detection of objects, for which we used the hierarchical peak-finding algorithm from Kaiser et al. (1995). We select objects that are detected with a significance greater than 5σ over the local sky. In addition to the positions of the objects, the peak finder also provides fair estimates of the object’s size. We use this information to remove all objects smaller than the PSF. Inspection shows that these are either extremely faint objects, or, more relevant, spurious detections of diffraction spikes, etc. The remaining objects are analysed in more detail, which yields estimates for the size, apparent magnitude, and shape parameters (polarization and polarizabilities). The apparent magnitudes are corrected for galactic extinction using the results from Schlegel et al. (1998).

The images were inspected by eye to mask out areas where the shape measurements could be compromised. Potential sources can be cosmic, such as bleeding stars, halos, diffraction spikes, but also astronomical, such as HII regions or spiral structure in resolved galaxies. We separate the stars and galaxies on the basis of their half-

light radii. The galaxy shapes are corrected for observational distortions as described below. The final, corrected, catalogs for each chip are combined into a large catalog for each field.

For the weak lensing analysis we use only galaxies brighter than $i'_{AB} = 24.5$, which leaves a sample of 9.7×10^5 galaxies in the W1 field and 6.5×10^5 galaxies in the W3 field. The surveyed area is $\sim 22 \text{ deg}^2$, resulting in an average galaxy number density of ~ 20 galaxies arcmin^{-2} . However, the shape measurement errors are larger for faint, small galaxies. Therefore these galaxies should be given less weight for an optimal estimate of the lensing signal (Hoekstra et al. 2000).

Instead it is more convenient to define an effective number density of galaxies n_{eff} , which is related directly to the measurement error in the shear for an area of 1 arcmin^2 , which is the relevant quantity. Hubble Space Telescope observations indicate that for well resolved galaxies the intrinsic shapes of galaxies results in a dispersion $\langle \gamma^2 \rangle^{1/2} \approx 0.3$ (Hoekstra et al. 2000). If all galaxies were measured ‘perfectly’, the error in the shear measurement would be given by $\sigma_\gamma = 0.3/\sqrt{n_{\text{eff}}}$. For the CFHTLS data this yields an effective number density of ~ 12 galaxies arcmin^{-2} .

3.1. Correction for PSF Effects

The observed shapes of the galaxies cannot be used to measure the lensing signal, because observational distortions have significantly altered their shapes in a systematic fashion: PSF anisotropy introduces coherent alignments in the galaxy shapes and the seeing circularizes the images. The key to an accurate measurement of the weak lensing signal lies in the adequate correction for these systematic effects. As mentioned above, our pipeline has been tested extensively (e.g., Hoekstra et al.

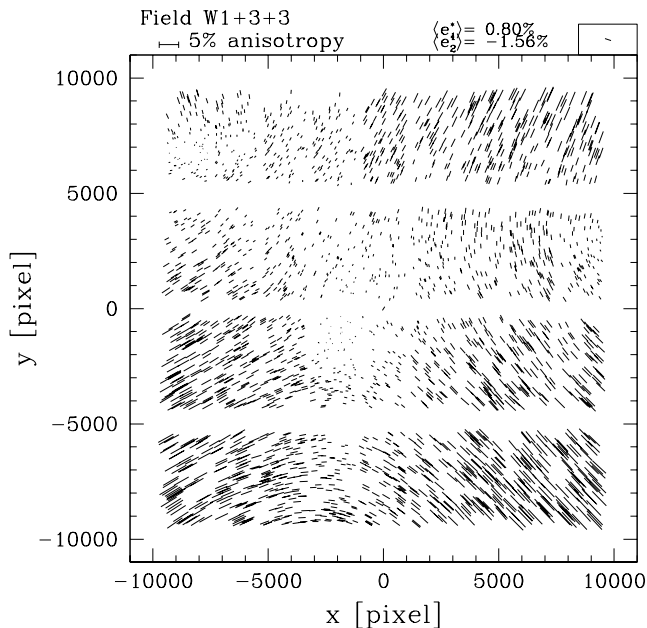


FIG. 3.— A typical example of the PSF anisotropy as a function of position for a stacked Megacam image. The sticks indicate the direction of the major axis of the PSF and the length is proportional to the observed ellipticity of the PSF. In order to show the higher order spatial dependence of the anisotropy, we have subtracted the average ellipticity. The direction of the average PSF anisotropy is indicated in the top right box and the amplitude is indicated as well. Although the PSF anisotropy is determined for individual chips, the figure clearly shows a large-scale coherent pattern.

2002b; Heymans et al. 2005) and has been shown to be able to recover the weak lensing shear with an accuracy of $\sim 2\%$.

The first step in this procedure is the identification of a sample of moderately bright stars which can be used to quantify the properties of the PSF (anisotropy and ‘size’). The pattern of PSF anisotropy changes from observation to observation, although we found that the Megacam PSF is relatively stable, in particular when compared to the previous CFH12k camera (e.g., Hoekstra 2004). The PSF anisotropy also varies across the field of view and this spatial variation is captured by fitting a second order polynomial to the shape parameters of the stars for each chip.

We found that a second order polynomial provided an excellent fit to the data. Note that the choice of model depends on the properties of the camera. For instance van Waerbeke et al. (2005) used rational functions (as suggested by Hoekstra (2004)) to describe the pattern of the CFH12k camera. We intend to improve our characterization following the procedure developed by Jarvis & Jain (2005), which combines information from a series of exposures, effectively resulting in a denser sampling of the PSF variation.

A typical example of the PSF anisotropy as a function of position across the Megacam mosaic is presented in Figure 3. To show the spatial variation in more detail, we have subtracted the mean anisotropy across the field. The resulting pattern is coherent across the field, even though the fits were obtained from individual chips.

Having quantified the PSF anisotropy and its spatial variation, we can undo its effect following Kaiser et al. (1995) and Hoekstra et al. (1998). The same stars used

to study the PSF anisotropy are also used to correct for the diluting effect of seeing, as described in Luppino & Kaiser (1997) and Hoekstra et al. (1998).

4. MEASUREMENTS

To quantify the lensing signal, we measure the ellipticity (or shear) correlation functions from the galaxy shape catalogs. These correlation functions, in turn, can be related to the various two-point statistics that are commonly used in the literature. The use of the ellipticity correlation functions also allow for the separation of the signal into ‘E’-mode (gradient) and ‘B’-mode (curl) components. Gravitational lensing arises from a gravitational potential and it is therefore expected that the lensing signal is curl-free. The amplitude of the ‘B’-mode then provides a measure of residual systematics.

In §5 we briefly discuss how these observable two-point statistics relate to the matter power spectrum and cosmology. For more detailed discussions we refer to Schneider et al. (1998) and Bartelmann & Schneider (2001). The two ellipticity correlation functions that are measured are

$$\xi_{tt}(\theta) = \frac{\sum_{i,j}^{N_s} w_i w_j \gamma_{t,i}(\mathbf{x}_i) \cdot \gamma_{t,j}(\mathbf{x}_j)}{\sum_{i,j}^{N_s} w_i w_j}, \quad (1)$$

and

$$\xi_{rr}(\theta) = \frac{\sum_{i,j}^{N_s} w_i w_j \gamma_{r,i}(\mathbf{x}_i) \cdot \gamma_{r,j}(\mathbf{x}_j)}{\sum_{i,j}^{N_s} w_i w_j}, \quad (2)$$

where $\theta = |\mathbf{x}_i - \mathbf{x}_j|$. γ_t and γ_r are the tangential and 45 degree rotated shear in the frame defined by the line connecting the pair of galaxies. The weights w_i are proportional to the inverse square of the uncertainty in the shear (Hoekstra et al. 2000). For the following, it is more useful to consider

$$\xi_{\pm}(\theta) = \xi_{tt}(\theta) \pm \xi_{rr}(\theta), \quad (3)$$

i.e., the sum and the difference of the two observed correlation functions. As shown by Crittenden et al. (2002), one can derive ‘E’ and ‘B’-mode correlation functions by integrating $\xi_+(\theta)$ and $\xi_-(\theta)$ with an appropriate window function

$$\xi^E(\theta) = \frac{\xi_+(\theta) + \xi'_+(\theta)}{2} \quad \text{and} \quad \xi^B(\theta) = \frac{\xi_+(\theta) - \xi'_+(\theta)}{2}, \quad (4)$$

where

$$\xi'_+(\theta) = \xi_-(\theta) + 4 \int_{\theta}^{\infty} \frac{d\vartheta}{\vartheta} \xi_-(\vartheta) - 12\theta^2 \int_{\theta}^{\infty} \frac{d\vartheta}{\vartheta^3} \xi_-(\vartheta). \quad (5)$$

We also present results for other frequently used two-point statistics, namely the aperture mass variance $\langle M_{\text{ap}}^2 \rangle(\theta)$ and the top-hat smoothed variance $\langle \gamma^2 \rangle(\theta)$.

Of these statistics, the aperture mass is of some particular interest, because only for this case are the ‘E’ and ‘B’-modes uniquely defined, whereas the decompositions of the shear correlation function and the top-hat variance in E and B modes are defined up to a constant (Crittenden et al. 2002; Pen et al. 2002). The aperture mass is defined as

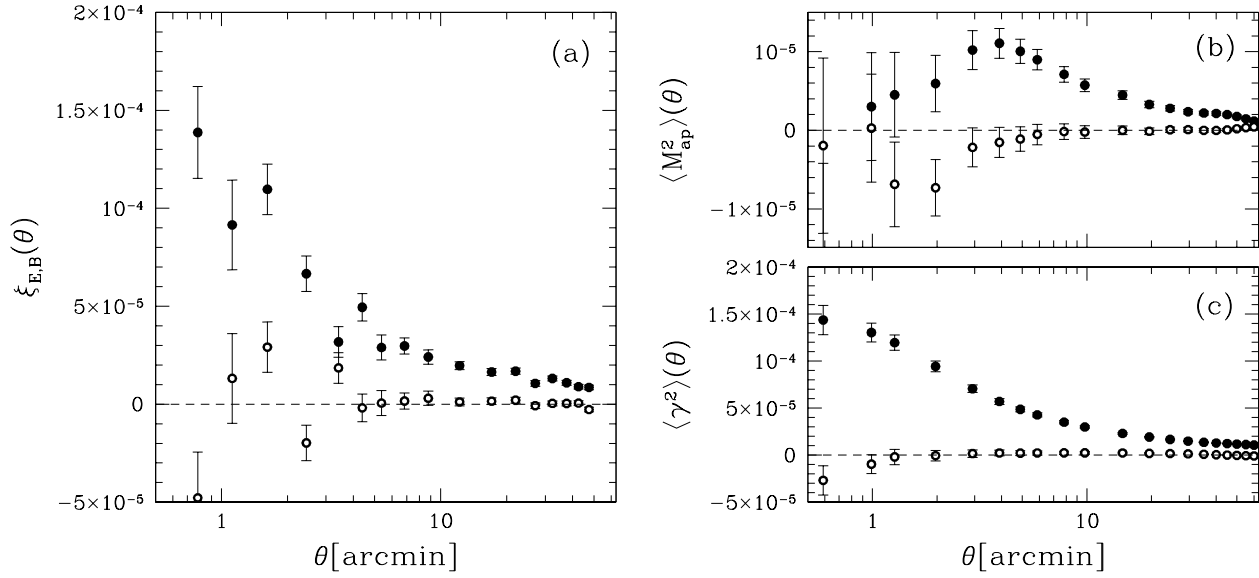


FIG. 4.— Panel a) ‘E’ and ‘B’-mode shear correlation functions (filled and open points, respectively) measured from $\sim 22 \text{ deg}^2$ of i' data from the CFHT Legacy Survey. The error bars only indicate the statistical errors determined for the combined signal from the data from W1 and W3 fields. Panel b) ‘E’ and ‘B’-mode measurements for the aperture mass statistic. Note that the ‘B’-mode is consistent with zero on all scales. Panel c) as before but now for the top-hat variance.

$$M_{\text{ap}}(\theta) = \int d^2\vartheta U(\vartheta) \kappa(\vartheta), \quad (6)$$

where κ is the dimensionless surface density or convergence. Provided $U(\vartheta)$ is a compensated filter (i.e., a filter such that a constant surface density within the aperture yields $M_{\text{ap}} = 0$), the aperture mass can be expressed in term of the observable tangential shear γ_t using a different filter function $Q(\vartheta)$ (which is a function of $U(\vartheta)$),

$$M_{\text{ap}}(\theta) = \int_0^\theta d^2\phi Q(\vartheta) \gamma_t(\vartheta). \quad (7)$$

We use the filter function suggested by Schneider et al. (1998)

$$U(\theta) = \frac{9}{\pi\theta^2} \left(1 - \frac{\vartheta^2}{\theta^2}\right) \left(\frac{1}{3} - \frac{\vartheta^2}{\theta^2}\right), \quad (8)$$

for $\theta \leq \vartheta$, and 0 elsewhere. The corresponding $Q(\theta)$ is given by

$$Q(\theta) = \frac{6}{\pi\theta^2} \left(\frac{\vartheta^2}{\theta^2}\right) \left(1 - \frac{\vartheta^2}{\theta^2}\right), \quad (9)$$

for $\theta \leq \vartheta$, and 0 elsewhere. The ‘E’ and ‘B’-mode aperture masses are computed from the ellipticity correlation functions using

$$\langle M_{\text{ap}}^2 \rangle(\theta) = \int d\vartheta \vartheta \left[\mathcal{W}(\vartheta) \xi_+(\vartheta) + \tilde{\mathcal{W}}(\vartheta) \xi_-(\vartheta) \right], \quad (10)$$

and

$$\langle M_{\perp}^2 \rangle(\theta) = \int d\vartheta \vartheta \left[\mathcal{W}(\vartheta) \xi_+(\vartheta) - \tilde{\mathcal{W}}(\vartheta) \xi_-(\vartheta) \right], \quad (11)$$

where $\mathcal{W}(\vartheta)$, and $\tilde{\mathcal{W}}(\vartheta)$ are given in Crittenden et al. (2002). Useful analytic expressions were derived by Schneider et al. (2002a). Both $\mathcal{W}(\vartheta)$, and $\tilde{\mathcal{W}}(\vartheta)$ vanish for $\vartheta > 2\theta$, so that $\langle M_{\text{ap}}^2 \rangle$ can be obtained directly from the observable ellipticity correlation functions over a finite interval. Similarly, the top-hat variance can be expressed in terms of the ellipticity correlation functions, but with different filter functions, as described in Schneider et al. (2002a).

4.1. Lensing signal

The results for the various two-point statistics are presented in Figure 4. The filled points in Figure 4a indicate the observed ‘E’-mode shear correlation function as a function of angular scale. The error bars indicate only the statistical uncertainty in the measured signal, and ignores any contribution from cosmic variance which is present in the ‘E’-mode signal. However, when estimating cosmological parameters, as discussed in §5, we include estimates for cosmic variance. The open points correspond to the ‘B’-mode. The signal presented in Figure 4 is based on the 22 deg^2 of data for the W1 and W3 fields.

As mentioned previously, in order to separate the signal into ‘E’ and ‘B’-modes, we have to define a zero-point for the ‘B’-mode for the shear correlation function and top-hat variance. Based on the absence of ‘B’-modes in the observed aperture mass variance, shown in Figure 4b, the correlated function in panel a has been scaled such that the mean ‘B’-mode is zero on scales larger than 10 arcminutes.

Figure 4c shows the top-hat variance $\langle \gamma^2 \rangle$ as a function of scale. All three statistics have been used in the past to estimate cosmological parameters, and each has its own distinct advantage and disadvantage. For instance the aperture mass provides an absolute calibration of the ‘B’-

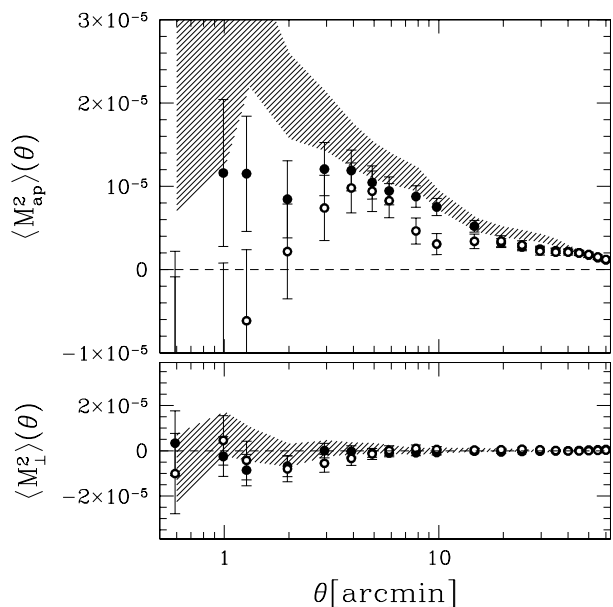


FIG. 5.— *top panel*: Aperture mass variance determined from W1 (solid points) and W3 (open points) separately. For reference, the shaded region indicates the 1σ area around the measurement from the VIRMOS-Descart survey (van Waerbeke et al. 2005), which is of similar depth. The W1 measurements agree well with the latter, but the W3 signal is lower than expected. On large scales (beyond 10 arcminutes) the agreement between all three measurements is excellent. Note, however, that the error bars do not include cosmic variance. *bottom panel*: Aperture mass ‘B’-mode for all three measurements, which are all consistent with no signal.

mode, but is most sensitive to the matter power spectrum on small scales. To probe the largest scales available in the surveyed area, we chose to use the top-hat variance for our estimates of cosmological parameters, presented in §5.

The results presented in Figure 4 combine the measurements of the W1 and W3 fields. However, it is useful to compare the signals obtained from the individual fields as well, to check for consistency. The aperture mass variances for the two fields are shown in the upper panel of Figure 5. The solid points correspond to W1, whereas the open points are for W3. For reference we also show the results from van Waerbeke et al. (2005), indicated by the shaded region. The latter uses a similar range in apparent magnitude, although the filter is different (I_C vs. i' used here). Hence the amplitude should be comparable to our measurements. On scales beyond 10 arcminutes all three measurements are in good agreement, but on small scales, the results from W3 appear lower than expected. The origin of this discrepancy is not clear, and increasing the surveyed area for this field might provide a better understanding. The lower panel of Figure 5 shows the corresponding ‘B’-modes, which are all consistent with zero on all scales.

This paper presents the first CFHTLS results based on one of two reduction and analysis pipelines. An independent analysis was performed by the Paris group and for reference we also show a comparison with their preliminary results in Figure 6. A detailed discussion of this alternative analysis will be presented in Fu et al. (in preparation). The top panels in Figure 6 show the aperture

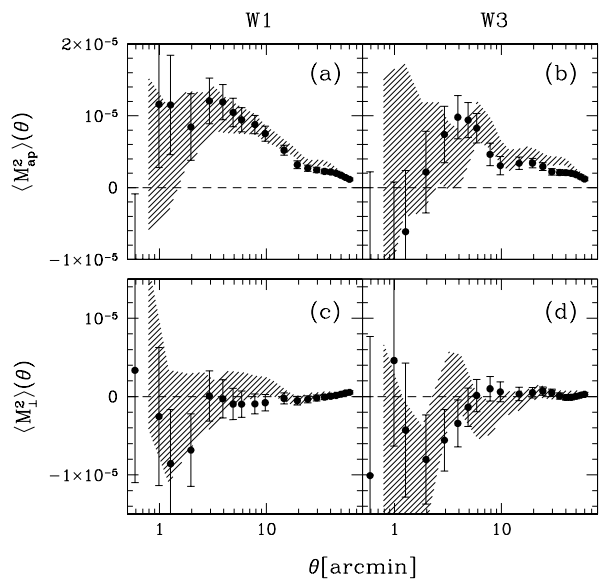


FIG. 6.— *panels a and b*: The aperture mass variance from the W1 and W3 fields, respectively. The points correspond to the results presented here. The shaded regions indicate the 1σ area around the measurements from the Paris pipeline (Fu et al., in preparation). *panels c and d*: The aperture mass ‘B’-mode signal for the W1 and W3 fields. The results from the two pipelines agree very well. Note, that the Paris results are based on a smaller survey area than the one presented in this paper.

mass variance for the W1 and W3 fields. The points correspond to the results from the analysis presented in this paper. The shaded regions indicate the 1σ area around the measurements from the Paris pipeline (Fu et al., in preparation). The lower panels show the corresponding measurements of the ‘B’-mode signals. The results from the two pipelines agree very well. We note, however, that the Paris results are based on conservatively masked images, resulting in a smaller effective survey area than the one presented in this paper.

4.2. Tests for Residual Systematics

The absence of a significant ‘B’-mode is very encouraging. However, by itself it cannot guarantee that the results are free of systematics (the presence of a ‘B’-mode provides strong evidence for residual systematics, but the converse is not true). Fortunately several other tests can be performed as well. These tests essentially provide additional checks on the correction for PSF anisotropy, and we present results in this section.

If the correction for the size of the PSF (i.e., seeing) is imperfect, this can result in calibration biases (e.g., Hirata & Seljak 2003). Unfortunately, there is no good test of this correction, based on the data alone. Instead, one needs to rely on comparison with simulated data sets, such as STEP (Heymans et al. 2005). As mentioned above, the results of the latter experiment suggests that we can recover the shear to better than 2%. We will assume a systematic error of this magnitude when estimating cosmological parameters.

Depending on the set of cosmological parameters one is interested in, one can marginalize over the uncertainty in this correction, with little loss in accuracy (Ishak et al.

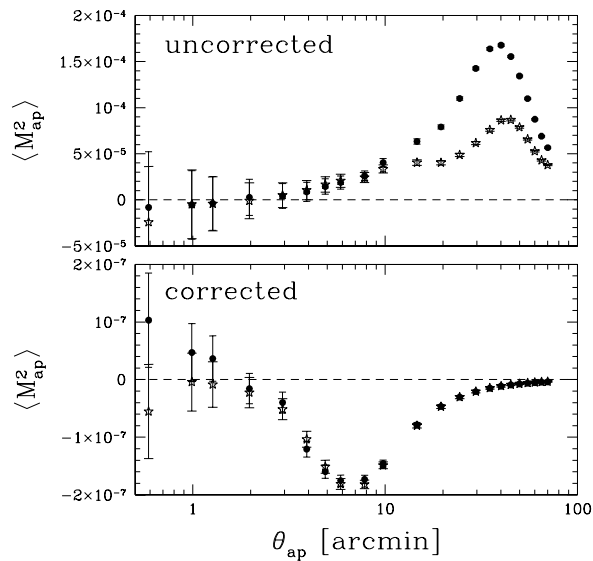


FIG. 7.— *top panel:* The aperture mass variance computed from the uncorrected shapes of the stars. The ‘E’-mode (solid points) and ‘B’-modes (stars) are very similar on scales < 10 arcminutes, but on larger scales the ‘E’-mode is larger. *bottom panel:* The aperture mass using the residual shapes of stars after correcting for PSF anisotropy. The ‘E’ and ‘B’ modes are indistinguishable on all scales. The results suggest that the adopted PSF model is inadequate on scales between 4 and 20 arcminutes. Note, however, that the lensing signal on these scales is ~ 30 times larger than the residuals presented here.

2004). This approach, however, may fail when studying the effect of massive neutrinos (e.g., Abazajian & Dodelson 2003). However, such an approach does not take into account the variable bias that might arise from pointing to pointing seeing variations. Fortunately, as shown in Vale et al. (2004), the signal is not affected significantly by small variations in calibration errors, thus reducing the complexity of the problem for current data sets.

As was shown in Hoekstra (2004) and van Waerbeke et al. (2005) the PSF anisotropy leads to a systematic signal which can have different ‘E’ and ‘B’-modes. For instance, the systematic ‘B’-mode was ~ 3 times lower than the systematic ‘E’-mode. Furthermore the source of an imperfect correction for PSF anisotropy can be twofold. First of all, the correction method itself might introduce errors. This has been studied in great detail (e.g. Hoekstra et al. 1998; Heymans et al. 2005) demonstrating that the correction scheme used here, is sufficiently accurate. Secondly, as pointed out in Hoekstra (2004), an incorrect model for the spatial variation of the PSF anisotropy can lead to considerable errors.

Recently, Jarvis & Jain (2005) have presented an interesting way to improve the PSF model using the large number of exposures taken in a weak lensing survey. They analyse the PSF variation using a principal component analysis to identify the dominant PSF anisotropy patterns. Under the assumption that only a few parameters are needed to describe most of the variation, this approach allows for a much more detailed modelling of the PSF. We plan to implement this method for future analyses of the CFHTLS data.

We can test both of these potential points of failure. The accuracy of the model describing the spatial vari-

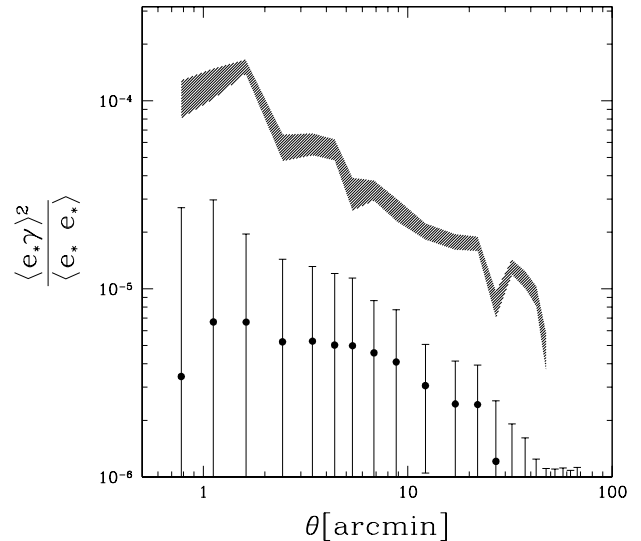


FIG. 8.— The points with error bars show the residual systematic correlation function ξ_{sys} as defined in the text. The indicated error bars are those of the shear correlation function, and are displayed to show the level of systematics with respect to the 1σ statistical error. The shaded region corresponds to the 1σ region around the observed shear correlation itself, which is an order of magnitude larger than ξ_{sys}

ation of the PSF anisotropy can be examined by correcting the measured shapes of the stars and computing the aperture mass variance of the residuals. In this case, any residual signal is caused by imperfections of the model (Hoekstra 2004). Figure 7 shows the results of this test. For reference, the upper panel shows the aperture mass variance of the stars before correction for PSF anisotropy. The ‘E’-mode (solid points) and ‘B’-modes (stars) are very similar on scales < 10 arcminutes, but on larger scales the ‘E’-mode is significantly larger. Given that this signal is larger than the cosmic shear signal on scales larger than 10 arcminutes, this figure clearly demonstrates the importance of a careful correction for PSF anisotropy.

The bottom panel of Figure 7 shows the aperture mass variance using the residual shapes of stars after they have been corrected for PSF anisotropy. The ‘E’ and ‘B’ modes are indistinguishable on all scales. The results clearly demonstrate that the adopted PSF model is inaccurate on scales between 4 and 20 arcminutes. Note, however, that the level of the residuals is about a factor of 30 smaller than the cosmic shear signal. Although there is clearly room for improvement regarding the modelling of the spatial variation of the PSF, the results presented in Figure 7 suggest that this is not a dominant source of error in our current analysis.

The next step is to examine how well the shapes of the background galaxies have been corrected. The amount of residual systematics left in the weak lensing signal due to imperfect PSF correction can be estimated from the correlation between the uncorrected stars and the corrected galaxies. Bacon et al. (2003) and Heymans et al. (2003) defined a useful estimator

$$\xi_{\text{sys}} = \frac{\langle e^* \gamma \rangle^2}{\langle e^* e^* \rangle}, \quad (12)$$

where e^* is the ellipticity of the stars before PSF correction and γ is the shear estimate of the galaxies. The estimator is conveniently normalized by the star ellipticity auto-correlation function, which allows for a direct comparison to the lensing signal $\langle \gamma(r) \gamma(\theta+r) \rangle$. Note that this estimator is sensitive to imperfections in the model for PSF anisotropy *and* imperfections in the correction scheme itself.

The points in Figure 8 correspond to the resulting value for ξ_{sys} as a function of scale. The indicated error bars are those of the shear correlation function, and are displayed to show the level of systematics with respect to the 1σ statistical error in the lensing signal. The shaded region corresponds to the 1σ region around the observed shear correlation itself, which is an order of magnitude larger than ξ_{sys} . These results demonstrate that the signal presented in Figure 4 is not significantly affected by systematics and can be used to provide reliable constraints on cosmological parameters. Note, however, as the CFHTLS progresses the level of residual systematics needs to be reduced.

5. COSMOLOGICAL PARAMETERS

The observed two-point statistics can be related to the matter power spectrum $P_\delta(k)$, which depends on a range of cosmological parameters. For the study presented here, the most relevant parameters are the matter density Ω_m and the normalisation σ_8 . In the case of cosmic shear, some of the dependence on cosmology also enters through the angular diameter distances to the sources.

5.1. Method

As discussed above, in order to probe the largest scales available in the surveyed area, we choose to use the top-hat variance $\langle \gamma^2 \rangle$, which can be expressed in terms of the power spectrum through

$$\langle \gamma^2 \rangle(\theta) = 2\pi \int_0^\infty dl l P_\kappa(l) \left[\frac{J_1(l\theta)}{\pi l \theta} \right]^2, \quad (13)$$

where θ is the radius of the aperture used to compute the variance, and J_1 is the first Bessel function of the first kind. $P_\kappa(l)$ is not the power spectrum itself, but the convergence power spectrum, defined as

$$P_\kappa(l) = \frac{9H_0^4 \Omega_m^2}{4c^4} \int_0^{w_H} dw \left(\frac{\bar{W}(w)}{a(w)} \right)^2 P_\delta \left(\frac{l}{f_K(w)}; w \right), \quad (14)$$

where w is the radial (comoving) coordinate, w_H corresponds to the horizon, $a(w)$ the cosmic scale factor, and $f_K(w)$ the comoving angular diameter distance. $\bar{W}(w)$ is the source-averaged ratio of angular diameter distances D_{ls}/D_s for a redshift distribution of sources $n(w)$:

$$\bar{W}(w) = \int_w^{w_H} dw' n(w') \frac{f_K(w' - w)}{f_K(w')}. \quad (15)$$

Hence, it is important to know the redshift distribution of the sources, in order to relate the observed lensing signal to $P_\kappa(l)$ and consequently, cosmological parameters.

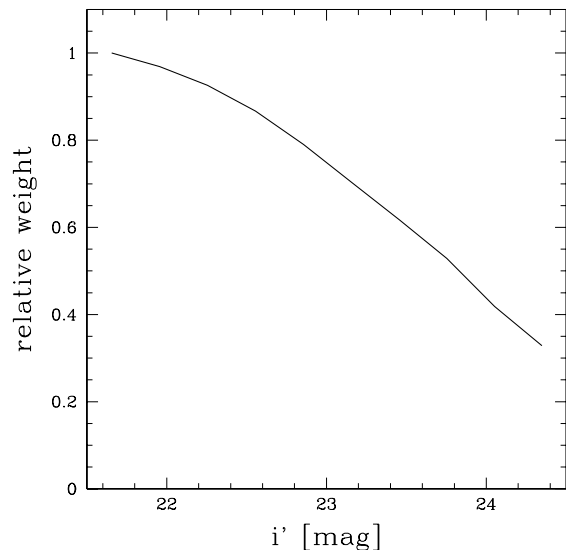


FIG. 9.— Average weight per galaxy as a function of apparent i' -magnitude. Note that the weights are not normalised

For our selection of background galaxies ($21.5 < i' < 24.5$), the redshift distribution should be very similar to the one used by van Waerbeke et al. (2005) in their analysis of the VIRMOS-Descart data. Currently, only i' images have been processed, but as the survey progresses photometric redshifts for the sources will be determined, which greatly enhances our ability to constrain the cosmology, and to minimize the uncertainty in the source redshift distribution.

Unfortunately, the current observational constraints on the redshift distribution are still limited, although a number of redshift surveys are targeting the faint galaxies and redshift range used for weak lensing (e.g., DEEP2: Davis et al. 2003; VVDS: Le Fèvre et al., 2004). For the analysis here, the best information on the source redshifts comes from photometric redshift studies of the Hubble Deep Fields (Fernández-Soto et al., 1999). It is convenient to parametrize the redshift distribution using

$$n(z) = \frac{\beta}{z_s \Gamma \left(\frac{1+\alpha}{\beta} \right)} \left(\frac{z}{z_s} \right)^\alpha \exp \left[- \left(\frac{z}{z_s} \right)^\beta \right]. \quad (16)$$

The best fit parameters are obtained from a least squares fit to the photometric redshift distribution, taking into account the adopted weights for the shape measurements of the sources (see the discussion in §4). The weight is predominantly a function of apparent magnitude and the average value is shown in Figure 9. As fainter galaxies are, on average, at higher redshift, such a weighting scheme will modify the true source redshift distribution into an ‘effective’ one. To compute the best fit parameters, we use the Poisson errors in the counts as a function of redshift, thus ignoring field-to-field variation in the HDF redshift distributions.

The solid histogram in Figure 10 shows the effective source redshift distribution. Comparison with the dashed histogram (which corresponds to the unweighted case) shows that the weighting scheme slightly lowers the

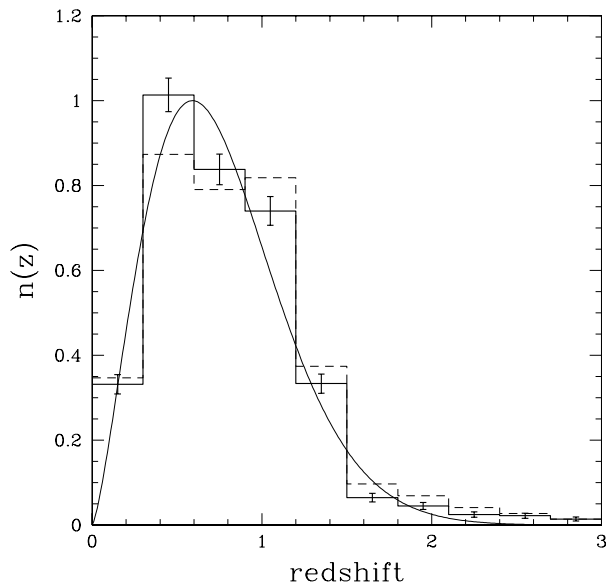


FIG. 10.— Effective redshift distribution of galaxies with $21.5 < I_{AB} < 24.5$ determined from the Hubble Deep Field North and South. The error bars are the Poisson errors from the finite number of galaxies in each bin (note that these do not include cosmic variance). The smooth solid curve represents the best fit model with a mean source redshift of $\langle z \rangle = 0.81$. The dashed histogram corresponds to the redshift distribution when the adopted weighting scheme is not taken into account.

mean source redshift. The smooth curve corresponds to the best fit redshift distribution, which has parameters $\alpha = 1.35$, $\beta = 1.654$ and $z_s = 0.668$. This corresponds to a mean source redshift of $\langle z \rangle = 0.81$. To quantify the uncertainties in the source redshift distribution, we keep α and β fixed, but vary z_s to identify the 68% and 95% confidence intervals. This yields $z_s \in [0.632, 0.703]$ with 68% confidence and $z_s \in [0.613, 0.721]$ with 95% confidence. We marginalise over the latter interval when estimating the cosmological parameters.

The scales probed by the measurement are affected significantly by the non-linear growth of structure. As shown by Jain & Seljak (1997) and Schneider et al. (1998), we cannot use the linear power spectrum, but it is necessary to use the non-linear power spectrum. Two different approaches to calculate the non-linear power spectrum have been proposed and we present results for both. The first is based on the scaling formula suggested by Hamilton et al. (1991), which was extended to a wider range of cosmologies by Peacock & Dodds (1996). Peacock & Dodds (1996) provide a prescription to compute the power spectrum, using a fitting formula which is calibrated using numerical simulations. More recently, Smith et al. (2003) suggested an approach based on a halo model approach to better capture the breakdown of the stable clustering assumption in the Peacock & Dodds (1996) prescription. We note that both prescriptions are based on relatively small numbers of numerical simulations and that their accuracy is limited. Comparison with recent numerical simulations suggest that they are accurate to $\sim 5\%$; this number depends on the region of parameter space that is probed and larger errors can occur (M. White, private communication).

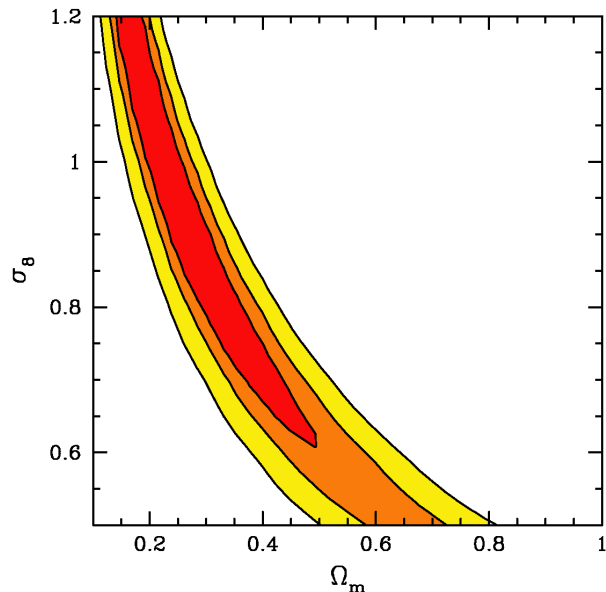


FIG. 11.— Joint constraints on Ω_m and σ_8 constraints from the CFHTLS Wide data using the Smith et al. (2003) model for the non-linear power spectrum. The contours indicate the 68.3%, 95.4%, and 99.7% confidence limits on two parameters jointly. We marginalised over the Hubble parameter and source redshift distribution as described in the text.

5.2. Constraints on Ω_m and σ_8

Cosmological parameters are estimated by comparing the predicted signal m_i to the observed top-hat variance d_i as a function of scale θ_i . We consider cold dark matter models with a flat geometry (i.e., $\Omega_m + \Omega_\Lambda = 1$). We vary the parameters of the model, focussing on constraining the matter density Ω_m and the normalisation σ_8 . For these parameters we limit the calculations to $\Omega_m \in [0, 1]$ and $\sigma_8 \in [0.5, 1.2]$.

As discussed above, we vary the source redshift distribution through $z_s \in [0.613, 0.721]$, assuming a flat prior. Furthermore, the signal depends somewhat on the value for the Hubble parameter, for which we use $h \in [0.6, 0.8]$ as motivated by the findings of the HST Key project (Freedman et al. 2001). In section §5.1 we also consider w_0 , the dark energy equation of state. The maximum likelihood function is given by

$$\mathcal{L} = \frac{1}{(2\pi)^n |\mathbf{C}|^{1/2}} \exp [-(d_i - m_i) \mathbf{C}^{-1} (d_i - m_i)^T]. \quad (17)$$

Here \mathbf{C}^{-1} is the covariance matrix. \mathbf{C} can be decomposed as $\mathbf{C} = \mathbf{C}_n + \mathbf{C}_s$, where \mathbf{C}_n is the statistical noise and \mathbf{C}_s the cosmic variance covariance matrix. The matrix \mathbf{C}_s is computed according to Schneider et al. (2002b), assuming an effective survey area of 13.5 deg^2 for the CFHTLS W1 and 8.5 deg^2 for W3, a number density of galaxies $n_{gal} = 12$ per arcmin^2 , and an intrinsic ellipticity dispersion of $\sigma_e = 0.3$ per component.

Figure 11 shows the joint constraints on Ω_m , σ_8 using the Smith et al. (2003) model for the non-linear power spectrum. For reference with other cosmic shear studies, we estimate the value of σ_8 for a fiducial matter density of $\Omega_m = 0.3$. For the Peacock & Dodds (1996) model,

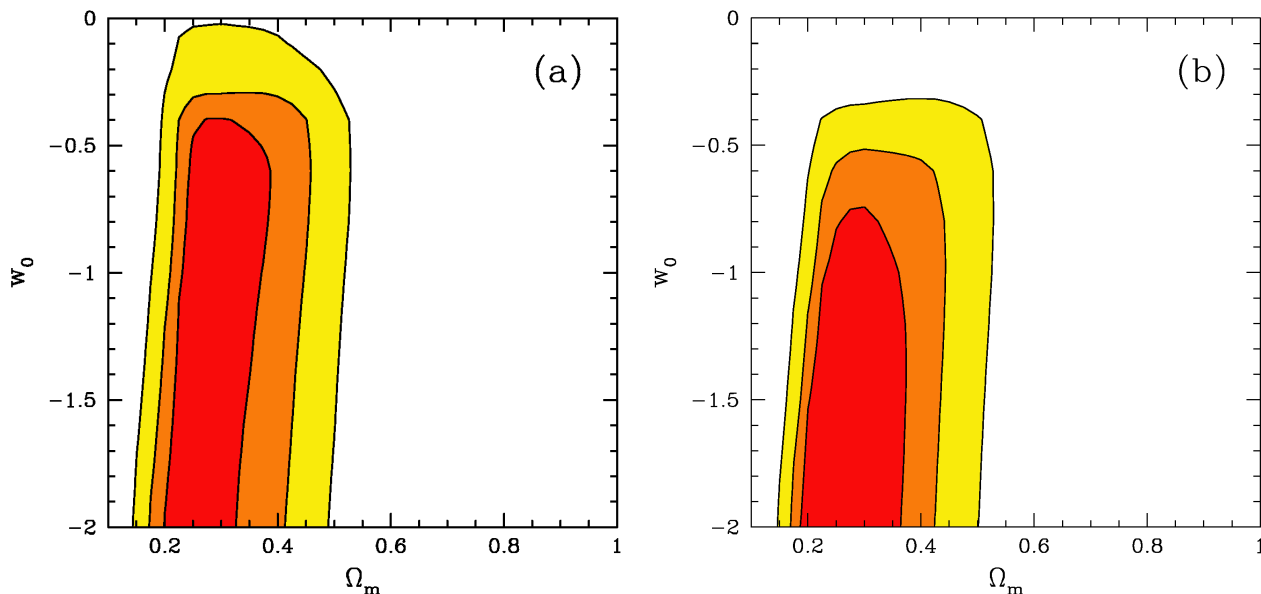


FIG. 12.— *panel a*: Dark energy constraints using the measurements from the W1 and W3 fields. The contours indicate the 68.3%, 95.4%, and 99.7% confidence limits on two parameters jointly. We marginalised over $\sigma_8 \in [0.7, 1.0]$, $h \in [0.6, 0.8]$ and the source redshift distribution as described in the text. *panel b* Results when the measurements from the Deep component (Semboloni et al. 2005) are included. We used the Peacock & Dodds (1996) prescription for the non-linear power spectrum.

we obtain a value of $\sigma_8 = 0.88 \pm 0.06$ (68% confidence). The error includes the statistical errors, cosmic variance and calibration errors. For the Smith et al. (2003) model we obtain a slightly lower value of $\sigma_8 = 0.85 \pm 0.06$. For $\Omega_m < 0.4$, the degeneracy between the two parameters is well described by $\sigma_8 \propto \Omega_m^{-0.6}$. The estimates for σ_8 based on the W1 and W3 separately also agree well. For $\Omega_m = 0.3$, we find $\sigma_8 = 0.87 \pm 0.07$ for W1 and $\sigma_8 = 0.75 \pm 0.12$ for W3.

These estimates are in excellent agreement with published cosmic shear results from other large surveys. Van Waerbeke et al. (2005) list a value of $\sigma_8 = 0.83 \pm 0.07$ based on the VIRMOS-Descart survey. Hoekstra et al. (2002c) obtained $\sigma_8 = 0.86^{+0.04}_{-0.05}$ from the Red-sequence Cluster Survey. Jarvis et al. (2005) found $\sigma_8 = 0.81^{+0.15}_{-0.10}$ (95% confidence) from the CTIO lensing survey. The constraints obtained here also agree well with those derived from the CFHTLS Deep survey and a detailed comparison as well as combined constraints with our measurements are presented in Semboloni et al. (2005).

5.3. Constraints on dark energy

One of the major goals of the CFHTLS is the measurement of the equation of state of dark energy. The current lack of (photometric) redshift information seriously limits the accuracy of such a measurement. Given the current limitations of the data, we choose a simple model with a constant equation of state:

$$p = w_0 \rho. \quad (18)$$

The left panel in Figure 12 shows the joint constraints on Ω_m and w_0 based on the measurements of the lensing signal from the W1 and W3 fields. We marginalised over $\sigma_8 \in [0.7, 1.0]$, $h \in [0.6, 0.8]$ and the source redshift distribution as described above and considered the

range of $-2 < w_0 < 0$. To obtain these results we used the Peacock & Dodds fitting formula to obtain the non-linear power spectrum. We emphasize that there is not yet a reliable analytical fit to the non-linear dark matter power spectrum available for non-trivial dark energy models. In particular, the halo model proposed in Smith et al. (2004) cannot provide an accurate description of the $w_0 \neq -1$ models because the power spectrum does not depend on w_0 at $z = 0$. We know that a change in w_0 should affect the background and therefore the change in structure clustering, which Smith et al. (2004) do not take into account. McDonald et al. (2005) have recently extended the halo-model to smaller scales for $w_0 \neq -1$ dark energy models. We will present a detailed dark energy measurement in a subsequent work, taking into account new model fitting to numerical simulations, and the CFHTLS type Ia supernovae constraints (Van Waerbeke et al., in preparation).

Although we currently lack photometric redshift information, the measurements of the Deep fields presented by Semboloni et al. (2005) probe the matter power spectrum at a slightly higher mean redshift, compared to the measurements presented here. Hence, we can improve our constraints on w_0 by combining our results to those obtained from the Deep survey (Semboloni et al. 2005). We stress that this should be considered a consistency check rather than a complete dark energy analysis. The result of this analysis is presented in the right panel of Figure 12, which gives $w_0 < -0.8$ with 68% confidence.

6. CONCLUSIONS

We have presented the first cosmic shear analysis based on $\sim 22 \text{ deg}^2$ (31 pointings) of deep i' imaging data from the CFHT Legacy Survey. These observations cover part of two of three survey fields and already provide a significant increase in area compared to previous work. These

early data show a strong variation of the PSF over the field of view. We note that recent changes to Megaprime have led to a significant reduction in PSF anisotropy. Nevertheless, our early results are very encouraging as we do not detect a significant ‘B’-mode, suggesting that the derived lensing signal is free of systematics at the current level of accuracy. Comparison with an independent pipeline (Fu et al., in preparation) shows good agreement and demonstrates that the signal can be recovered robustly.

We assume a cold dark matter model with a flat geometry and derive joint constraints on the matter density Ω_m and the normalisation of the matter power spectrum σ_8 , while marginalising over the Hubble parameter and the source redshift distribution. We consider two models to calculate the non-linear power spectrum. For a fiducial matter density of $\Omega_m = 0.3$ we find $\sigma_8 = 0.88 \pm 0.06$ for the Peacock & Dodds (1996) model. Similarly, we obtain a value of $\sigma_8 = 0.85 \pm 0.06$ using the Smith et al. (2003) approach. These estimates are in excellent agreement with previous studies (Hoekstra et al. 2002c; Jarvis et al. 2005; van Waerbeke et al. 2005).

In the coming years we expect to image a total ~ 140 deg² in five filters, allowing us to include photometric redshift information for the source galaxies. This will greatly enhance our ability to constrain cosmological pa-

rameters, most notably the equation of state of the dark energy (e.g., see forecasts in Tereno et al., 2005). The measurements from Semboloni et al. (2005), based on the Deep component of the CFHTLS probe a higher mean source redshift, thus providing crude redshift leverage. When combining our results with the measurements from Semboloni et al. (2005) we find $w_0 < -0.8$ (68% confidence) based on cosmic shear measurements alone.

We acknowledge use of the Canadian Astronomy Data Centre, which is operated by the Dominion Astrophysical Observatory for the National Research Council of Canada’s Herzberg Institute of Astrophysics. HH thanks Dave Balam and Stephen Gwyn for discussions on astrometry. YM, ES, IT and LF thank the CNRS-INSU and the “French Programme National de Cosmologie” for their support to the CFHTLS cosmic shear program. ES thanks the University of British Columbia for hospitality. LF thanks the “European Association for Research in Astronomy” training site (EARA) and the European Community for the Marie Curie doctoral fellowship MEST-CT-2004-504604. HH, MJH and LvW are supported by NSERC. HH and LvW acknowledge support by the the Canadian Institute for Advanced Research (CIAR) and the Canadian Foundation for Innovation (CFI).

REFERENCES

- Abazajian, A. & Dodelson, S. 2003, PRL, 91, 1301
 Bacon, D.J., Refregier, A., & Ellis, R.S. 2000, MNRAS, 318, 625
 Bacon, D.J., Refregier, A., Clowe, D. & Ellis, R.S. 2001, MNRAS, 325, 1065
 Bacon, D.J., Massey, R.J., Refregier, A.R., Ellis, R.S. 2003, MNRAS, 344, 673
 Bartelmann, M., & Schneider, P. 2001, Physics Reports, 340, 291
 Benabed, K. & van Waerbeke, L. 2004, PhRvD, 7013515
 Bernstein, G.M. & Jarvis, M. 2002, AJ, 123, 583
 Bertin, E. & Arnouts, S. 1996, A&AS, 117, 393
 Brainerd, T.G., Blandford, R.D., & Smail, I. 1996, ApJ, 466, 623
 Contaldi, C.R., Hoekstra, H., & Lewis, A. 2003, PRL, 90, 1303
 Clowe, D., Luppino, G.A., Kaiser, N., Henry, J.P., & Gioia, I.M. 1998, ApJ, 497, L61
 Crittenden, R.G., Natarajan, P., Pen, U.-L., & Theuns, T. 2002, ApJ, 568, 20
 Cypriano, E.S., Sodré, L., Kneib, J.-P. & Campusano, L.E. 2004, ApJ, 613, 95
 Dahle, H., Kaiser, N., Irgens, R.J., Lilje, P.B., & Maddox, S.J. 2002, ApJS, 139, 313
 Davis, M. et al. 2003, in “Discoveries and Research Prospects from 6- to 10-Meter-Class Telescopes II”, Edited by Guhathakurta, Puragra. Proceedings of the SPIE, Volume 4834, pp. 161-172, astro-ph/0209419
 Erben, T., Van Waerbeke, L., Bertin, E., Mellier, Y., Schneider, P. 2001, MNRAS, 366, 717
 Fernández-Soto, A., Lanzetta, K.M., & Yahil, A. 1999, ApJ, 513, 34
 Freedman, W.L., et al. 2001, ApJ, 553, 47
 Hamilton, A.J.S., Kumar, P., Lu, E., & Matthews, A. 1991, ApJ, 374, L1
 Heymans, C., 2003, PhD thesis.
 Heymans, C. et al. 2005, MNRAS, submitted, astro-ph/0506112
 Hirata, C. & Seljak, U. 2003, MNRAS, 343, 459
 Hoekstra, H., Franx, M., Kuijken, K. & Squires, G. 1998, ApJ, 504, 636
 Hoekstra, H., Franx, M., Kuijken, K. 2000, ApJ, 532, 88
 Hoekstra, H., Franx, M., Kuijken, K. & van Dokkum, P.G. 2002a, MNRAS, 333, 911
 Hoekstra, H., Yee, H.K.C., Gladders, M.D., Barrientos, L.F., Hall, P.B., & Infante, L. 2002b, ApJ, 572, 55
 Hoekstra H., Yee, H.K.C., & Gladders, M.D 2002c, ApJ, 577, 595
 Hoekstra, H. 2004, MNRAS, 347, 1337
 Hoekstra H., Yee, H.K.C., & Gladders, M.D 2004, ApJ, 606, 67
 Hudson, M.J., Gwyn, S.D.J., Dahle, H., & Kaiser, N. 1998, ApJ, 503, 531
 Ishak, M., Hirata, C., McDonald, P., Seljak, U. 2004, PhRvD, 69, 83514
 Jain, B., & Seljak, U. 1997, ApJ, 484, 560
 Jarvis, M., Bernstein, G.M., Fischer, P., Smith, D., Jain, B., Tyson, J.A. & Wittman, D. 2003, AJ, 125, 1014
 Jarvis, M. & Jain, B. 2005, ApJ, submitted, astro-ph/0412234
 Jarvis, M., Jain, B., Bernstein, G.M. & Dolney, D. 2005, astro-ph/0502243
 Kaiser, N., Squires, G., & Broadhurst, T. 1995, ApJ, 449, 460
 Kaiser, N., Wilson, G., & Luppino, G.A. 2000, ApJL, submitted, astro-ph/0003338
 Le Fèvre et al. 2004, A&A, 428, 1043
 Luppino, G.A., Kaiser, N., 1997, ApJ, 475, 20
 McDonald, P., Trac, H., & Contaldi, C. 2005, astro-ph/0505565
 McKay, T.A., et al. 2001, ApJ, submitted, astro-ph/0108013
 Peacock, J.A., & Dodds, S.J. 1996, MNRAS, 780, L19
 Pen, U.-L., Van Waerbeke, L., Mellier, Y., 2002, ApJ, 567, 31
 Refregier, A. 2003, MNRAS, 338, 35
 Schlegel, D.J., Finkbeiner, D.P., & Davis, M. 1998, ApJ, 500, 525
 Schneider, P., van Waerbeke, L., Jain, B., & Kruse, G. 1998, MNRAS, 296, 873
 Schneider, P., van Waerbeke, L. & Mellier, Y. 2002a, A&A, 389, 729
 Schneider, P., van Waerbeke, L., Kilbinger, M., & Mellier, Y. 2002b, A&A, 396, 1
 Semboloni et al. 2005, A&A, submitted, astro-ph/0511090
 Smith, R. E., Peacock, J. A., Jenkins, A., White, S. D. M., Frenk, C. S., Pearce, F. R., Thomas, P. A., Efstathiou, G., Couchman, H. M. P. 2003, MNRAS, 341, 1311
 Tereno, I., Doré, O., van Waerbeke, L., & Mellier, Y. 2005, A&A, 429, 383
 Vale, C., Hoekstra, H., van Waerbeke, L. & White, M. 2004, ApJ, 613, L1
 van Waerbeke, L., et al. 2000, A&A, 358, 30
 van Waerbeke, L., Mellier, Y. & Hoekstra, H. 2005, A&A 429, 75
 Wittman, D.M., Tyson, J.A., Kirkman, D., Dell’Antonio, I., & Bernstein, G. 2000, Nature, 405, 143